FREE for Reading & Publication
Diamond Open Access

Low Resistance and High Electromigration Lifetime of Cu-To-Cu Joints Using (111)-Oriented Nanotwinned Copper

Jing-Ye Juang[1], Kai Cheng Shie[1], Yu Jin Li[1], K. N. Tu[1,2], Chih Chen[1,]*

Cu-to-Cu joints of 30 μm in diameter were fabricated using (111)-oriented nanotwinned copper at 300 °C for 20 min in N_2 ambient. The joints possess excellent electrical properties. The average resistance and specific contact resistivity are 4.1 mΩ and 3.98 × 10^{-8} Ω·cm^2, respectively for an as-fabricated Cu joint. With a second step annealing at 400 °C, the resistance can be reduced to 3.27 mΩ due to grain growth across the joint interface. There is 50% resistance reduction compared to SnAg solder joints with the same diameter. The electromigration lifetime for Cu-to-Cu joints is at least 750 times longer than solder joints.

Introduction

Solder microbumps have been adopted for vertical interconnects between stacked chips in 3D IC technology, because of the advantage of low melting point and self-alignment process [**1-4**]. Currently, the dimension of the microbumps is about 20 μm, and it is continually scaled down due to the high I/O demand in the microelectronic industry. When the solder microbumps shrink its size, the volume percentage of brittle Cu-Sn or Ni-Sn intermetallic compounds (IMCs) increases, resulting in yield and reliability issues [**5-9**]. It is reported that the solder microbumps could not scale down below 10 μm in diameter. In addition, open failure occurs easily in solder joints with small solder volume during electromigration and solid state aging [**10-12**]. Therefore, an alternative solution for ultra-fine pitch packaging is desperately needed.

Cu-to-Cu direct bonding has emerged to be the best solution for the ultra-fine pitch packaging, because Cu microbumps can be fabricated below 1 μm and it has excellent electrical and thermal properties [**13**]. For example, Cu microbumps has been implemented in CMOS image sensors of mobile devices, and they will be also adopted to be vertical interconnection of stacked high-bandwidth memory (HBM) chips [**14,15**]. Previous studies reported that the Cu-to-Cu direct bonding can be achieved under a vacuum or ambient atmosphere [**16-21**]. Some researchers adopted plasma pre-treatments [**22**] or metal capping approach [**23**] to lowering bonding temperatures, while others using nanotwinned Cu to achieve low temperature (under 250 °C) bonding [**24,25**]. However, the electrical properties of the Cu joints are not well-understood. In this study, we fabricated (111)-oriented nanotwinned Cu (nt-Cu) microbumps with 30 μm in diameter, and performed a two-step Cu-to-Cu direct bonding technique to achieve excellent bonding and grain growth to eliminate bonding interfaces. Subsequently, resistance measurement by Kelvin probes and electromigration (EM) tests on the Cu joints were conducted to evaluate its electrical performance. The results show that the Cu joints possess superior electrical properties than the SnAg solder joints with the similar dimension.

Experimental

To fabricate Cu-to-Cu joints, arrays of (111)-oriented nt-Cu microbumps were electroplated on both the top and bottom dies. The dimensions of the test samples are 6 mm × 6 mm for the top die and 15 mm × 15 mm for the bottom die. The die thickness for both top and bottom dies is 500 μm. The nt-Cu microbumps are 30 μm in diameter and 10 μm in height. The diameter of the Cu microbumps can be smaller than 5 μm when a better lithography process is adopted. Owing to the rough surfaces of the as-plated nt-Cu microbumps, chemical-mechanical-polishing (CMP) process was performed to planarize the Cu microbump surfaces. After the CMP process, the root mean square roughness (R_q) was ranging from 3 nm to 5 nm. Daisy chains with 400 Cu-to-Cu joints and Kelvin structures were designed into the test samples, so that we can measure the chain loop resistance and single joint resistance after the direct bonding process. Before the direct bonding process, wet etching was performed to remove organic contaminants and the oxide layer. The test dies were rinsed with deionized water, followed by a short immersion in a mixed solution of citric acid and deionized water (in the ratio

[1]Department of Materials Science and Engineering, National Chiao Tung University, Hsinchu, Taiwan 30010, ROC
[2]Department of Materials Science and Engineering, University of California at Los Angeles, Los Angeles, California 90095, USA

*Corresponding author:
E-mail: chih@mail.nctu.edu.tw
Tel.: (+886) 3 5731814; Fax: (+886) 3 5724727

DOI: 10.5185/amlett.2021.081654

133 g/100 ml) at 60 °C for about 30 sec. Then, they were rinsed again with deionized water and dried by N_2 purging before bonding.

Cu-to-Cu direct bonding with a two-step process was applied. In the first step, thermal compression bonding with a pressure of 64 MPa was performed in a N_2 purging atmosphere with a temperature gradient between the top and bottom die. The top die was at 300 °C and the bottom die was at 100 °C. The bonding time is 20 min. Subsequently, the bonded samples were subjected to an annealing bonding under 400 °C in a vacuum oven for 60 min to trigger grain growth across the bonding interfaces.

Scanning electron microscope (SEM) incorporated with focused ion beam (FIB) was employed to observe the microstructures of the Cu-to-Cu joints. Electron backscattered diffraction (EBSD) was performed to acquire Cu grain orientation (JSM-7800F scanning electron microscope with Nordlys Max3 EBSD detector). Aztec EBSD post-processing software was employed to provide statistical orientation maps and crystallographic textures. For EM tests, we applied the Cu joints and SnAg joints with 2.12×10^5 A/cm^2 on a hotplate maintained at 150 °C. The joint resistance was monitored throughout the entire testing period using the Kelvin probes. When the resistance reached to 120% of its initial value, the current was terminated and the samples were then subjected to cross-sectioning process for the microstructure analysis.

Results and discussion

Fig. 1(a) shows the nt-Cu microbumps array after the surface planarization process. The dimension of the microbumps is 30 µm in diameter and 10 µm in height. **Fig. 1(b)** shows the cross-sectioned FIB image of an nt-Cu microbump. Columnar grains with densely-packed lamellae nanotwins can be observed. In addition, the orientation of surface grains is analyzed by EBSD, and the orientation map in **Fig. 1(c)** shows the distribution of grain orientations of a Cu microbump. Approximately 65% of surface area is occupied by the (111) oriented grains, which is shown in blue color. The (111) plane of Cu possesses a high surface diffusivity, so that the nt-Cu microbumps enables a low-temperature or fast process bonding via surface creep [**26-28**].

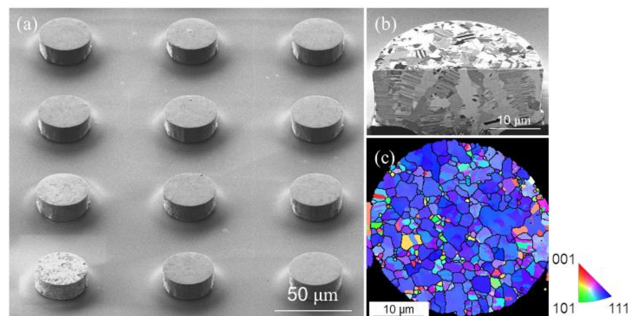

Fig.1. (a) SEM image showing the arrays of nt-Cu microbumps after CMP. (b) Cross-sectional FIB image for a nt-Cu microbump composed of columnar grains with dense lamella nanotwins (c) Plan-view EBSD orientation image map showing 65% of surface grains are (111)-oriented.

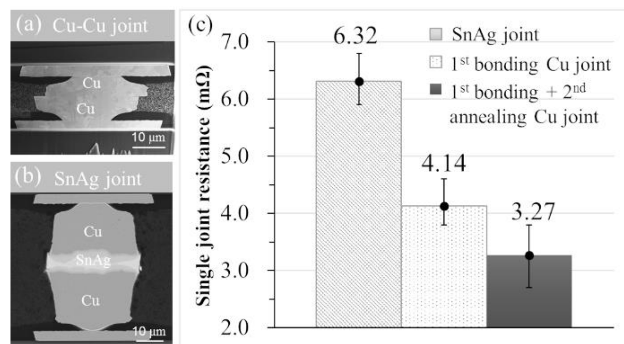

Fig. 2. Cross-sectional SEM image for (a) Cu joint, and (b) SnAg joint. (c) Measured average resistance for a SnAg solder joint, an as-bonded Cu joint, a Cu joint after the second annealing.

The Cu joints possess a low resistance and specific contact resistivity. **Fig. 2(a)** presents the as-bonded Cu joints at 300 °C for 20 min. The resistance measurement was conducted using the Kelvin structures after the first. For comparison of electrical properties, arrays of SnAg microbumps with the same diameter were also fabricated, as depicted in **Fig. 2(b)**. The solder thickness is approximately 10 µm and the Cu under-bump-metallization (UBM) is 20 µm in height. After the first bonding process, the mean resistance for a Cu joint is 4.14 mΩ, and the contact resistivity is 3.98×10^{-8} Ω·cm^2, which is the product of a joint resistance and contact area. However, the average resistance for a SnAg joint is 6.32 mΩ, as shown in **Fig. 2(c)**. Therefore, the Cu joints have 34% resistance reduction compared to the SnAg solder joints. It is noteworthy to mention that the height of the solder joint in **Fig. 2(b)** is 45 µm, while it is only 15 µm for the Cu joint.

The electrical resistance of the Cu joints can be further reduced by the second step annealing. The average resistance for a Cu joint decreases to 3.27 mΩ. Its specific contact resistivity also drops to 3.14×10^{-8} Ω·cm^2. The low specific contact resistivity represents that most of the bonding interface has excellent contact and free of Cu oxides. With the aid of the second annealing process, the Cu joint possesses a resistance reduction of 48% compared to the solder joint. **Table 1** listed the comparison of specific contact resistance from several reference. In reference [**31**], the value of 10^{-8} Ω·cm^2 was the limitation of cross Kelvin resistors measurement.

Table 1. Comparison of specific contact resistance.

Reference	Specific contact resistance (Ω.cm^2)	Bonding methods
[29]	7×10^{-4}	Ti passivation
[30]	2×10^{-7}	Pd passivation
[23]	2×10^{-7}	Cr wetting layer and Au passivation layer
[31]	$>10^{-8}$	If specific contact resistance is lower than 10^{-8} Ω.cm^2, quality of Cu-to-Cu bonding is too excellent to be easily measured.
Current study	3.98×10^{-8}	Cu-to-Cu direct bonding with N_2 purging atmosphere
Current study	3.14×10^{-8}	After second step annealing

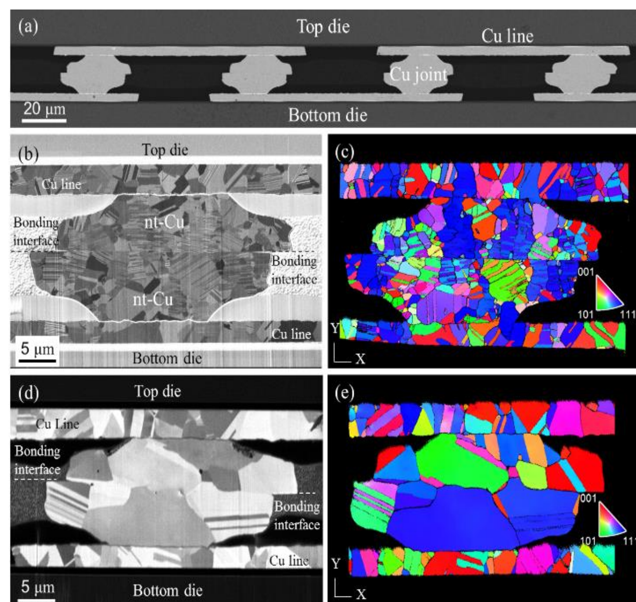

Fig. 3. Microstructure changes before and after the second annealing. (a) Cross-sectional SEM image of the Cu joints in the daisy chain loop, (b) Cross-sectional FIB image, and (c) Corresponding EBSD image for the Cu joint in (b) after the 1st direct bonding process. (d) Cross-sectional FIB image, and (e) Corresponding EBSE image for the Cu joint in (d) after the 2nd annealing process.

To investigate the microstructure changes responsible for the resistance reduction after the second annealing process, microstructure analysis on the Cu joint before and after annealing process was carried out by FIB and EBSD. **Fig. 3(a)** shows the cross-sectional SEM image of the Cu joints in the daisy chain loop. All the 400 Cu joints can be successfully bonded. **Fig. 3(b)** shows one of the Cu joints with very few nanoscale voids at the bonding interface after the first bonding process. These voids have no obvious effect on rising of contact resistance. In addition, no obvious Cu oxide layers were found. **Fig. 3(c)** shows the corresponding orientation map (OIM) and the inverse pole figure was shown in lower right corner. The orientation shown in **Fig. 3** was along the Y direction. It was found that the nanotwinned columnar grains remained in the Cu joint, yet a clear bonding interface can be observed. After the second step annealing, a significant microstructure change was identified. Recrystallization and grain growth phenomena were observed, as shown in **Fig. 3(d)**. Most of the nanotwinned grains disappeared and new sets of large grains formed, resulting in less grain boundaries. Besides, the grain growth eliminated the original bonding interface. The newly grown grains were <111>-, <101>-, and <100>-oriented, as presented in the cross-sectional OIM images in **Fig. 3(e)**. The resistance of a Cu joint reduced from 4.14 mΩ to 3.27 mΩ after the second annealing. We speculated that the removal of the original bonding interface is the main cause for the reduction in resistance and specific contact resistivity.

The Cu joints also possess much longer electromigration lifetime than the solder joints. **Fig. 4(a)** presents the resistance increase as a function of time up to 750 h for a Cu joint by 2.12×10^5 A/cm^2 at 150 °C. The resistance almost did not increase. However, for the same stressing conditions, the solder joint failed within 1 h, as shown in **Fig. 4(b)**. The resistance increased over 100 % of its initial value. Therefore, the electromigration lifetime of the Cu joint is at least 750 times longer than the solder joint. **Fig. 4(c)** and **Fig. 4(d)** show the cross-sectional SEM image for the Cu and SnAg solder joint after the electromigration test, respectively. The electron flow drifted from the top to the bottom Cu ones, as indicated by the arrows in the figures. No failure or void formation was found in the Cu joint. However, open failure in the SnAg joint was observed, which was attributed by side- diffusion of the Sn atoms. [**16-18**]. The Sn atoms diffused to the side walls of the Cu metallization bumps and depleted the solder joint. This is because Sn has a very low melting point of 232 °C. Copper has been known to have high electromigration lifetimes for its high melting point of 1084 °C and high yield strength, and thus it has been adopted for damascene Cu lines [**32,33**]. When grain growth takes place to remove the bonding interface, the Cu joint has high electromigration resistance.

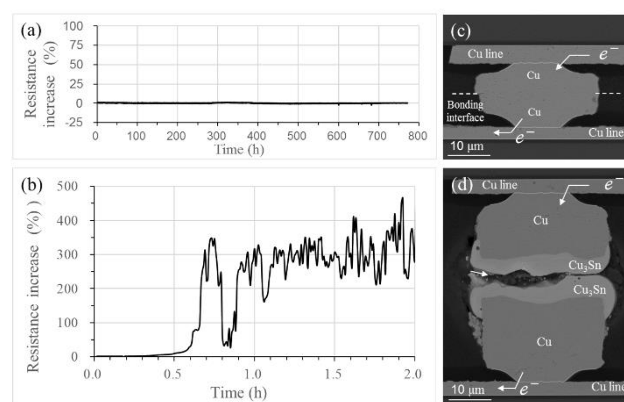

Fig. 4. Electromigration tests and failure analysis for the Cu and SnAg solder joints. The monitored resistance curves against stressing time for (a) A Cu joint (b) A SnAg joint. (c) SEM image of the Cu joint after electromigration test by 2.12×10^5 A/cm^2 at 150 ºC for 750 h; (b) SEM image showing the open failure after 2.12×10^5 A/cm^2 at 150 ºC for 2 h.

More reliability issues need to be investigated in urgent, because the Cu joints have been implemented in real devices. But there are very few literatures addressing on these issues. For example, electromigration failure mechanisms needs to be understood, so that researchers can find ways to prolong their lifetimes. In addition, other reliabilities, such as temperature cycling and drop tests has not been studied. Finally, how the bonding interface and interfacial voids affect the electromigration, and temperature cycling, and drop tests are of high interests.

Conclusion

In summary, Cu-to-Cu direct bonding by using the (111) oriented nt-Cu has been achieved in N_2 ambient. The as-bonded Cu joint showed a low resistance value of 4.12 mΩ and 3.98×10^{-8} Ω·cm^2 in contact resistivity. With the aid of

a second step annealing, the resistance and the contact resistivity can be further reduced to 3.27 mΩ and 3.14×10^{-8} Ω·cm^2, respectively. There is nearly 50% resistance reduction, as compared to the SnAg solder joint. During the second annealing at 400 °C, recrystallization and grain growth took place, resulting in the annihilation of the original bonding interface and thus better electrical properties. In addition, the Cu joints possess a longer electromigration lifetime (at least 750 times) than the SnAg solder joints. In future, Cu-to-Cu joints will be scaled down, so the current density would increase continuously. The reliability issue of EM would be more vital for 3D IC development. Therefore, the Cu-to-Cu joints have superior electrical performance and have the potential to be used as interconnects for ultra-fine pitch and low power devices.

Acknowledgements

This work was financially supported by the "Center for the Semiconductor Technology Research" from The Featured Areas Research Center Program within the framework of the Higher Education Sprout Project by the Ministry of Education (MOE) in Taiwan; the Ministry of Science and Technology, Taiwan, under Grant MOST-109-2634-F-009-029, MOST-107-2221-E-009-007-MY3, and MOST-109-2639-E-009-001.

Conflicts of interest

The authors declare that they have no known competing financial interests

Keywords

Cu-to-Cu direct bonding, nanotwinned Cu, grain growth, electromigration, resistance.

Received: 10 December 2020
Revised: 18 March 2021
Accepted: 27 March 2021

References

1. Knickerbocker, J.U.; Andry, P.S.; Dang, B.; Horton, R.R.; Interrante, M.J.; Patel, C.S.; Polastre, R.J.; Sakuma, K.; Sirdeshmukh, R.; Sprogis, E.J.; Sri-Jayantha, S.M.; Stephens, A.M.; Topol, A.W.; Tsang, C.K.; Webb, B.C.; Wright, S.L.; *IBM J. Res. Dev.,* **2008**, *52,* 553.
2. Zhan, C.J.; Chuang, C.C.; Juang, J.Y.; Lu, S.T.; Chang, T.C.; Proc. 60th Electron. Components Technol. Conf., IEEE, **2010**, 1043-1049.
3. Huebner, H.; Penka, S.; Barchmann, B.; Eigner, M.; Gruber, W.; Nobis, M.; Janka, S.; Kristen, G.; Schneegans, M.; *Microelectron. Eng.,* **2006**, *83,* 2155.
4. Wright, S.L.; Polastre, R.; Gan, H.; Buchwalter, L.P.; Horton, R.; Andry, P.S.; Sprogis, E.; Patel, C.; Tsang, C.; Knickerbocker, J.; Lloyd, J.R.; Sharma, A.; Sri-Jayantha, M.S. 56th Electron. Components Technol. Conf. IEEE, **2006**, 633-640.
5. Lu, S.T.; Juang, J.Y.; Cheng, H.C.; Tsai, Y.M.; Chen, T.H.; Chen, W.H.; IEEE Trans. Device Mater. Reliab., **2012**, *12,* 296-305.
6. Zhou, B.; Bieler, T.R.; Lee, T.K.; Liu, W.; *J. Electron. Mater.,* **2013**, *42,* 319.
7. Jang, J.W.; Frear, D.R.; Lee, T.Y.; Tu, K.N.; *J. Appl. Phys.,* **2000**, *88,* 6359.
8. Chen, Y.J.; Chung, C.K.; Yang, C.R.; Kao, C.R.; *Microelectron. Reliab.,* **2013**, *53,* 47.
9. Philippi, B.; Matoy, K.; Zechner, J.; Kirchlechner, C.; Dehm, G.; *Scr. Mater.,* **2016**, *123,* 38.
10. Liang, Y.C.; Chen, C.; Tu, K.N.; *ECS Solid State Lett.,* **2012**, *1,* 60.
11. Chen, C.; Yu, D.; Chen, K. N.; MRS Bull., **2015**, 40, pp526-529.
12. Chang, Y. W.; Hu, C.; Peng, H. Y.; Liang, Y. C.; Chen, C.; Chang, T.; Zhan, C. J.; Juang, J. Y.; *Sci. Rep.,* **2018**, *8,* 5935.
13. Kim, S.W.; Fodor, F.; Heylen, N.; Iacovo, S.; Vos, J.D.; Miller, A.; Beyer, G.; Beyne, E.; 2020 Proc. 70th Electron. Components Technol. Conf., IEEE, **2020**, 216-222.
14. Kagawa, Y.; Iwamoto, H.; Int. 3D Syst. Integration Conf., **2019**, 1-4.
15. Fujun, B.; Xiping, J.; Song, W.; Bing, Y.; Jie, T.; Fengguo, Z.; Chunjuan, W.; Fan, W.; Xiaodong, L.; Guoqing, Y.; Ni, F.; Qiannan, L.; Hua, L.; Kexin, W.; Huifu, D.; Liang, B.; Xuerong, J.; Jin, L.; Mei, L.; Zhengwen, W.; Sheng, H.; Jun, Z.; Qiong, Z.; Peng, S.; Daohong, Y.; Kau, C.; Yang, D.; Ho, C.S.; Hongbin, S.; Hangbing, L.; Ming, L.; Yi, K.; Qiwei, R.; 2020 IEEE Int. Electron Devices Meet., **2020**, 6.6.1-6.6.4..
16. Hu, X.; Li, Y.; Liu, Y.; Liu, Y.; Min, Z.; *Microelectron. Reliab.,* **2014**, *54,* 1575.
17. Kagawa, Y.; Fujii, N.; Aoyagi, K.; Kobayashi, Y.; Nishi, S.; Todaka, N.; Takeshita, S.; Taura, J.; Takahashi, H.; Nishimura, Y.; Tatani, K.; Kawamura, M.; Nakayama, H.; Nagano, T.; Ohno, K.; Iwamoto, H.; Kadomura, S.; Hirayama, T.; 2016 IEEE Int. Electron Devices Meet., **2016**, 8.4.1-8.4.4.
18. Michailos, J.; Coudrain, P.; Farcy, A.; Hotellier, N.; Cheramy, S.; Lhostis, S.; Deloffre, E.; Sanchez, Y.; Jouve, A.; Guyader, F.; Saugier, E.; Fiori, V.; Vivet, P.; Vinet, M.; Fenouillet-Beranger, C.; Casset, F.; Batude, P.; Breuf, F.; Henrion, Y.; Vianne, B.; Collin, L. M.; Colonna, J. P.; Benaissa, L.; Brunet, L.; Prieto, R.; Velard, R.; Ponthenier, F. 2016 Int. Electron Devices Meet., **2016**, 8.5.1-8.5.4.
19. Beyne, E.; Kim, S. W.; Peng, L.; Heylen, N.; DeMessemaeker, J.; Okudur, O. O.; Phommahaxay, A.; Kim, T. G.; Stucchi, M.; Velenis, D.; Miller, A.; Beyer, G. 2017 IEEE Int. Electron Devices Meet., **2017**, 32.4.1-32.4.4.
20. Gao, G.; Mirkarimi, L.; Fountain, G.; Wang, L.; Uzoh, C.; Workman, T.; Guevara, G.; Mandalapu, C.; Lee, B.; Katkar, R. 2018 IEEE 68th Electron. Components Technol. Conf., IEEE, **2018**, 314–322.
21. Suga, T.; Mu, F. 2018 7th Electron. Syst. Technol. Conf., IEEE, **2018**, 1-4.
22. Seo, H.; Park, H.; Kim, S.E.; IEEE Trans. on Components, Packaging and Manufacturing Technol., **2020**, 10(11), 1814-1820.
23. Liu, D.; Chen, P.C.; Chen, K.N.; 2020 Proc. 70th Electron. Components Technol. Conf., IEEE, **2020**, 1322-1327.
24. Chiu, W.L.; Chou, K.W.; Chang, H.H.; Nanotwinned Copper Hybrid Bonding and Wafer-On-Wafer Integration, 2020 Proc. 70th Electron. Components Technol. Conf., IEEE, **2020**, 210-215.
25. Wu, Y S; Lai, T-Y; Li, M; Lu, T-F; Wang, Y H; Tseng, T Y; *ECS J. of Solid State Science and Technol.,* **2020**.
26. Liu, C. M.; Lin, H. W.; Huang, Y. S.; Chu, Y. C.; Chen, C.; Lyu, D. R.; Chen, K. N.; Tu, K. N.; *Sci. Rep.,* **2015**, *5,* 9734.
27. Juang, J. Y.; Lu, C. L.; Li, Y. J.; Tu, K. N.; Chen, C.; *Materials,* **2018**, *11,* 2368.
28. Juang, J. Y.; Lu, C. L.; Chen, K. J.; Chen, C. C. A.; Hsu, P. N.; Chen, C.; Tu, K. N.; *Sci. Rep.,* **2018**, *8,* 13910.
29. Huang, Y.; Chien, Y.; Tzeng, R.; Shy, M.; Lin, T.; Chen, K.; Chiu, C.; Chiou, J.; Chuang, C.; Hwang, W.; Tong, H.; Chen, K.; *IEEE Electron Device Lett.,* **2013**, *34,* 1551.
30. Huang,Y.; Chien, Y.; Tzeng, R.; Chen, K.; *IEEE Trans. on Electron Devices,* **2015**, *62,* 2587.
31. Jourdon, J.; Lhostis, S.; Moreau, S.; Bresson, N.; Salomé, P.; Frémont, H.; *IEEE Trans. on Electron Devices,* **2019**, *66,* 2699.
32. Ogawa, E. T.; Lee, K. D.; Blaschke, V. A.; Ho, P. S.; *IEEE Trans. Reliab.,* **2002**, *51,* 403.
33. Tu, K. N.; *Phys. Rev. B.,* **1992**, *45,* 1409.